A Numerical and Experimental Investigation of Period-*n* Bifurcations in Milling

Andrew Honeycutt
Department of Mechanical Engineering and Engineering Science,
University of North Carolina at Charlotte,
Charlotte, NC 28223-0001

Tony Schmitz
Department of Mechanical Engineering and Engineering Science,
University of North Carolina at Charlotte,
Charlotte, NC 28223-0001
e-mail: tony.schmitz@uncc.edu

Numerical and experimental analyses of milling bifurcations, or instabilities, are detailed. The time-delay equations of motions that describe milling behavior are solved numerically and once-per-tooth period sampling is used to generate Poincaré maps. These maps are subsequently used to study the stability behavior, including period-n bifurcations. Once-per-tooth period sampling is also used to generate bifurcation diagrams and stability maps. The numerical studies are combined with experiments, where milling vibration amplitudes are measured for both stable and unstable conditions. The vibration signals are sampled once-per-tooth period to construct experimental Poincaré maps and bifurcation diagrams. The results are compared to numerical stability predictions. The sensitivity of milling bifurcations to changes in natural frequency and damping is also predicted and observed. [DOI: 10.1115/1.4034138]

Keywords: milling, stability, Poincaré section, bifurcation diagram, time domain simulation

Introduction

Many years of machining research have led to a comprehensive understanding of milling process dynamics. As early as 1946, Arnold studied chatter in steel machining [1]. Doi and Kato described self-excited vibrations using time-delay differential equations in 1956 [2]. During this time, the notion of "regeneration of waviness" was promoted as the feedback mechanism (time-delay term), where the previously cut surface combined with the instantaneous vibration state dictates the current chip thickness, force level, and corresponding vibration response [3–6]. This work resulted in analytical algorithms that were used to produce the now well-known stability lobe diagram that separates the spindle speed–chip width domain into regions of stable and unstable behavior [6–17].

In 1998, Davies et al. used once-per-revolution sampling to characterize the synchronicity of cutting tool motions with the tool rotation in milling [18]. This approach was an experimental modification of the Poincaré maps used to study state-space orbits in nonlinear dynamics. They observed the traditional quasi-periodic chatter associated with the secondary (subcritical) Hopf, or Neimark-Sacker, bifurcation that can occur for systems described by periodic time-delay differential equations [19].

In 2000, Davies et al. further examined the stability of highly interrupted (or low radial immersion) milling [20]. They reported a doubling of the number of optimally stable spindle speeds when the time in cut is small (i.e., low radial depth of cut). In 2001, Moon and Kalmár-Nagy reviewed the "prediction of complex, unsteady and chaotic dynamics" in machining [19]. They listed the various contributors to nonlinear behavior, including the loss of tool–workpiece contact due to large amplitude vibration and workpiece material constitutive relations, and highlighted previous applications of nonlinear dynamics methods to the study of chatter [21–26]. They also specified the use of phase-space methods, such as Poincaré maps, to identify changes in machining process dynamics.

Time domain simulation offers a powerful tool for exploring milling behavior and has been applied to identify instability [27–28]. For example, Zhao and Balachandran implemented a time domain simulation, which incorporated loss of tool–workpiece contact and regeneration to study milling [29]. They identified secondary Hopf bifurcation and suggested that "period-doubling bifurcations are believed to occur" for low radial immersions. They included bifurcation diagrams for limited axial depth of cut ranges at two spindle speeds to demonstrate the two bifurcation types.

Davies et al. extended their initial work in 2002 to present the first analytical stability boundary for highly interrupted machining [30]. It was based on modeling the cutting process as a kicked harmonic oscillator with a time delay and followed the two-stage map concept described previously [20]. They used the frequency content of a microphone signal to establish the existence of both secondary Hopf and period-2 (period-doubling or flip) instabilities. Mann et al. also provided experimental validation of secondary Hopf and period-2 instabilities for up and down milling [31]. They reported "a kind of period triple phenomenon" observed using the once-per-revolution sampled displacement signal recorded from a single degree-of-freedom flexure-based machining platform.

The semidiscretization, time finite element analysis, and multi-frequency methods were also developed to produce milling stability charts that demonstrate both instabilities [32–36]. In Ref. [37], it was shown using the semidiscretization method that the period-2 bifurcation exhibits closed, lens-like, curves within the secondary Hopf lobes, except for the highest speed stability lobe. The same group reported further experimental evidence of quasi-periodic (secondary Hopf), period-2, period-3, period-4, and combined quasi-periodic and period-2 chatter, depending on the spindle speed–axial depth values for a two degree-of-freedom dynamic system [38]. A perturbation analysis was performed in Ref. [39] to identify the secondary Hopf and period-2 instabilities. Additionally, numerical integration was implemented to construct a bifurcation diagram for a selected spindle speed that demonstrated the transition from stable operation to quasi-periodic chatter as the axial depth is increased.

Stépán et al. continued to explore the nonlinear aspects of milling behavior in 2005 [40]. They described stable period-2 motion where the tool does not contact the workpiece in each tooth period (even in the absence of runout). For a two flute cutter, for example, only one tooth contacts the workpiece per revolution; they referred to this condition as the "fly over effect" and included a bifurcation diagram for these proposed stable and unstable period-2 oscillations.

Manuscript received March 8, 2016; final manuscript received June 30, 2016; published online August 8, 2016. Assoc. Editor: Radu Pavel.

The effect of the helix angle on period-2 instability was first studied by Zatarain et al. [41]. They found that, depending on the helix angle, the closed, lens-like, curves within the secondary Hopf lobes change their size and shape. They also found that these closed islands of stability can appear even in the highest speed stability lobe (in contrast to the results when helix angle is not considered). Experimental results were provided. This work was continued in Ref. [42], where the authors emphasized that, at axial depths equal to the axial pitch of the cutter teeth, the equation of motion becomes an autonomous delay differential equation so the period-2 instability is not possible. Patel et al. also studied the helix effect in up and down milling using the time finite element approach [43].

In this paper, time domain (numerical) simulation is used to predict milling dynamics. Periodic sampling of the milling signals is then applied to identify the presence of period-n bifurcations, in additional to the well-known quasi-periodic instability. Experiments are performed using flexure-based setups and the results are compared to time domain predictions. Period-n bifurcations are predicted and experimentally verified for $n = 2$, 3, 6, 7, 8, and 15. Additionally, the sensitivity of the bifurcation behavior to system dynamics, including both natural frequency and damping, is explored using both numerical simulation and experiments. The paper presents experimental evidence of new period-n bifurcations and, therefore, provides another step forward in the rich progression of machining science over the past decades.

Time Domain Simulation

Time domain simulation enables the numerical solution of the coupled, time-delay equations of motion for milling in small time steps. It is well suited to incorporating all the intricacies of milling dynamics, including the nonlinearity that occurs if the tooth leaves the cut due to large amplitude vibrations and complicated tool geometries (including runout, or different radii, of the cutter teeth, nonproportional teeth spacing, and variable helix). The simulation is based on the Regenerative Force, Dynamic Deflection Model described by Smith and Tlusty [27]. As opposed to stability maps that provide a global picture of the stability behavior, time domain simulation provides information regarding the local cutting force and vibration behavior (at the expense of computational efficiency) for the selected cutting conditions. The simulation used in this study proceeds as follows (see Fig. 1):

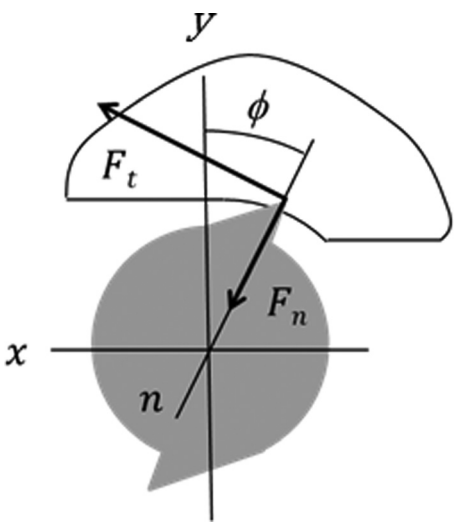

Fig. 1 Milling simulation geometry. The normal and tangential direction cutting forces, F_n and F_t, are identified. The fixed *x* and *y* directions, as well as the rotating normal direction, *n*, are also shown. The angle ϕ defines the tooth angle. The tool feed is to the right for the clockwise tool rotation and the axial depth is in the *z* direction.

(1) the instantaneous chip thickness is determined using the vibration of the current and previous teeth at the selected tooth angle
(2) the cutting force components in the tangential (t) and normal (n) directions are calculated using

$$\begin{aligned} F_t(t) &= k_{tc} b h(t) + k_{te} b \\ F_n(t) &= k_{nc} b h(t) + k_{ne} b \end{aligned} \tag{1}$$

where b is the axial depth of cut, $h(t)$ is the instantaneous chip thickness, and the cutting force coefficients are identified by the subscripts t or n for direction and c or e for cutting or edge effect.
(3) the force components are used to find the new displacements by numerical solution of the differential equations of motion in the x (feed) and y directions

$$\begin{aligned} m_x \ddot{x} + c_x \dot{x} + k_x x &= F_t(t)\cos(\phi) + F_n \sin(\phi) \\ m_y \ddot{y} + c_y \dot{y} + k_y y &= F_t(t)\sin(\phi) - F_n \cos(\phi) \end{aligned} \tag{2}$$

where m is the modal mass, c is the modal viscous damping coefficient, and k is the modal stiffness. The subscripts identify the direction and multiple degrees-of-freedom in each direction can be accommodated.
(4) the tool rotation angle is incremented and the process is repeated.

The instantaneous chip thickness depends on the nominal, tooth angle-dependent chip thickness, the current vibration in the direction normal to the surface, and the vibration of previous teeth at the same angle. The chip thickness can be expressed using the circular tooth path approximation as

$$h(t) = f_t \sin(\phi) + n(t - \tau) - n(t) \tag{3}$$

where f_t is the commanded feed per tooth, ϕ is the tooth angle, n is the normal direction (see Fig. 1), and τ is the tooth period. The tooth period is defined as

$$\tau = \frac{60}{\Omega N_t} \text{ (s)} \tag{4}$$

where Ω is the spindle speed in rpm and N_t is the number of teeth. The vibration in the direction of the surface normal for the current tooth depends on the x and y vibrations as well as the tooth angle according to

$$n = x \sin(\phi) - y \cos(\phi) \tag{5}$$

For the simulation, the strategy is to divide the angle of the cut into a discrete number of steps. At each small time-step, dt, the cutter angle is incremented by the corresponding small angle, $d\phi$. This approach enables convenient computation of the chip thickness for each simulation step because: (1) the possible teeth orientations are predefined; and (2) the surface created by the previous teeth at each angle may be stored. The cutter rotation

$$d\phi = \frac{360}{\text{SR}} \text{ (deg)} \tag{6}$$

depends on the selection of the number of steps per revolution (SR). The corresponding time-step is

$$dt = \frac{60}{\text{SR} \cdot \Omega} \text{ (s)} \tag{7}$$

A vector of angles is defined to represent the potential orientations of the teeth as the cutter is rotated through one revolution of the circular tool path, $\phi = [0, d\phi, 2\,d\phi, 3\,d\phi, \ldots, (\text{SR} - 1)\,d\phi]$. The locations of the teeth within the cut are then defined by referencing entries in this vector.

In order to accommodate the helix angle for the tool's cutting edges, the tool may be sectioned into a number of axial slices. Each slice is treated as an individual straight tooth end mill, where the thickness of each slice is a small fraction, db, of the axial depth of cut, b. Each slice incorporates a distance delay

$$r\chi = db\tan(\gamma) \tag{8}$$

relative to the prior slice (nearer the cutter free end), which becomes the angular delay between slices

$$\chi = \frac{db\tan(\gamma)}{r} = \frac{2db\tan(\gamma)}{d}\ (\text{rad}) \tag{9}$$

for the rotating end mill, where d is the end mill diameter and γ is the helix angle. In order to ensure that the angles for each axial slice match the predefined tooth angles, the delay angle between slices is

$$\chi = d\phi \tag{10}$$

This places a constraint on the db value. By substituting $d\phi$ for χ and rearranging, the required slice width is

$$db = \frac{d\cdot d\phi}{2\tan(\gamma)} \tag{11}$$

Using the time domain simulation approach [44], the forces and displacements may be calculated. These results are then sampled once-per-tooth period to generate Poincaré maps, bifurcation diagrams, and stability maps. These are described in the following three sections.

Poincaré Maps

Poincaré maps were developed using both experiments and simulations. For the experiments, the displacement and velocity of a flexible workpiece (the tool dynamic stiffness was much higher) were recorded and then sampled once-per-tooth period. In simulation, the displacement and velocity were predicted, but the same sampling strategy was applied. By plotting the displacement versus velocity, the phase space trajectory could be observed in both cases. The once-per-tooth period samples were then superimposed and used to interrogate the milling process behavior. For stable cuts, the motion is periodic with the tooth period, so the sampled points repeat and a single grouping of points is observed. When secondary Hopf instability occurs, the motion is quasi-periodic with tool rotation because the chatter frequency is (generally) incommensurate with the tooth passing frequency. In this case, the once-per-tooth sampled points do not repeat and they form an elliptical distribution. For period-2 instability, the motion repeats only once every other cycle (i.e., it is a subharmonic of the forcing frequency). In this case, the once-per-tooth sampled points alternate between two solutions. For period-n instability, the sampled points appear at n distinct locations in the Poincaré map.

Bifurcation Diagrams

In the bifurcation diagrams developed for this study, the once-per-tooth sampled displacement (vertical axis) was plotted against the axial depth of cut (horizontal axis). The transition in stability behavior from stable (at low axial depths) to period-n or secondary Hopf instability (at higher axial depths) is then directly observed. This diagram represents the information from multiple Poincaré maps over a range of axial depths, all at a single spindle speed. A stable cut appears as a single point (i.e., the sampled points repeat when only forced vibration is present). A period-2 bifurcation, on the other hand, appears as a pair of points offset from each other in the vertical direction. This represents the two collections of once-per-tooth sampled points from the Poincaré map. A secondary Hopf bifurcation is seen as a vertical distribution of points; this represents the range of once-per-tooth sampled displacements from the elliptical distribution of points in the Poincaré map.

Stability Maps

Stability maps, or stability lobe diagrams, identify the limiting axial depth of cut (vertical axis) as a function of spindle speed (horizontal axis). Traditionally, this limit is represented as a single contour which separates stable (forced vibration only) from unstable (secondary Hopf or period-n) parameter combinations. This map provides a global view of the stability behavior, but does not identify the type of instability. Because a bifurcation diagram presents the stability behavior as a function of axial depth, but only at one spindle speed, it can be considered as a high fidelity vertical slice of a stability map. Conversely, a stability map can be interpreted as a series of bifurcation diagrams where a binary switching function is used to categorize the behavior represented by the vertical distribution of once-per-tooth sampled points as either stable or unstable.

In this work, the binary stability is identified using a new stability metric, M, based on once-per-tooth sampling [45]. The metric builds on the approach in Ref. [46–48] where the standard deviation of the periodically sampled milling audio signal was calculated. The new stability metric is

$$M = \frac{\sum_{i=2}^{N} x_s(i) - x_s(i-1)}{N} \tag{12}$$

where x_s is the vector of once-per-tooth sampled x (feed direction) displacements and N is the length of the x_s vector. Other variables, such as y displacement (perpendicular to x in the plane of the cut) or cutting force could be selected as well. With this new stability metric, the absolute value of the differences in successive sampled points is summed and then normalized. Because the sampled points repeat for a stable cut (forced vibration), the M value is ideally zero. For unstable cuts, however, $M > 0$.

Experimental Validation of Period-*n* Bifurcations

In this section, comparison is made between time domain simulation predictions and milling experiments for multiple setups; the presence of period-n bifurcations, as well as their sensitivity to the structural dynamics, is presented. A single degree-of-freedom (SDOF) flexure was used to define the system dynamics, where the SDOF flexure was much less stiff than the cutting tool [31]. The flexure setup also simplified the measurement instrumentation. The flexure motions were measured using a capacitance probe (CP), laser vibrometer (LV), and low mass accelerometer. In order to enable once-per-tooth sampling of the vibration signals, a laser tachometer (LT) was used. A small section of reflective tape was attached to the tool holder and the corresponding (digital) tachometer signal was used to perform the periodic sampling.

The cutting tool was a 19.1 mm diameter, single flute carbide square end mill (30 deg helix angle). Modal impact testing verified that the cutting tool dynamic stiffness (1055 Hz natural frequency, 0.045 viscous damping ratio, and 4.2×10^7 N/m stiffness) was much higher than the SDOF flexure. Cutting tests were completed using Fig. 2 setup. The measured flexure dynamics and cutting conditions are listed in Table 1. Each cut of the 6061-T6 aluminum workpiece was performed using a feed per tooth of 0.10 mm/tooth. The aluminum alloy cutting force coefficients were: $k_{tc} = 792\times10^6$ N/m^2, $k_{nc} = 352\times10^6$ N/m^2, $k_{te} = 26\times10^3$ N/m, and $k_{ne} = 28\times10^3$ N/m.

Results for period-2, 3, 6, 7, and 8, and 15 bifurcations are displayed in Figs. 3–9. In each figure, the left plot shows the

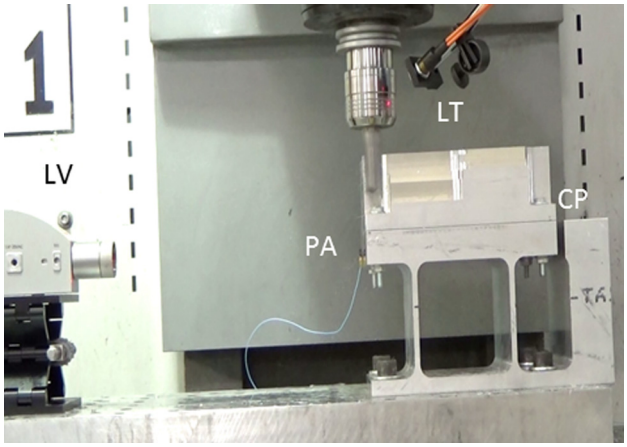

Fig. 2 Milling experimental setup with LV, piezo-accelerometer (PA), LT, and CP

simulated behavior and the right plot shows the experimental result, where the cut entry and exit transients were removed before plotting. Good agreement is observed in each case.

A bifurcation diagram for a spindle speed of 3800 rpm and radial depth of 5 mm was predicted by simulation and then cuts were performed from 1 mm to 7 mm axial depths in 0.5 mm steps. The CP displacement signal was sampled using the LT to construct an experimental bifurcation diagram; Fig. 10 provides the comparison between prediction and experiment. For this axial depth of cut range, period-3 bifurcations were observed (see the period-3 entry from Table 1 for the flexure dynamics).

A simulated stability map for the same axial depth of cut range as Fig. 10, but spindle speeds from 3300 rpm to 4300 rpm is displayed in Fig. 11 (the same dynamics were again used). The diagram was constructed by completing time domain simulations over a grid with a spindle speed resolution of 10 rpm and an axial depth resolution of 0.1 mm. The initial transients were removed and the M value for each simulation was calculated (see Eq. 1). An arbitrarily small value of 1 μm was selected to differentiate between stable and unstable parameter combinations; this contour is shown in Fig. 11 and identifies the stability limit. The transition from stable to unstable behavior at 3800 rpm observed in Fig. 10 is replicated. The transition from secondary Hopf to period-3 to secondary Hopf seen in the bifurcation diagram is not detailed in the stability map, however.

Sensitivity to Natural Frequency

Experiments were completed to demonstrate the sensitivity of the period-n bifurcation behavior to changes in natural frequency. During the cutting trials, material was removed from the workpiece. This lowered the workpiece mass and, subsequently, increased the flexure's natural frequency. Since the mass of the chips is much smaller than the workpiece, this material removal resulted in small changes in natural frequency. The variation in system dynamics for the results presented in Figs. 12–15 is provided in Table 2. The higher period-n bifurcations exhibited sufficient sensitivity to flexure natural frequency that, within a single cut, both period-n bifurcation and quasi-periodic behavior (secondary Hopf bifurcation) were observed. For these tests, the cutting tool was a 19.1 mm diameter, single flute carbide square end mill (30 deg helix angle). The cutting tool dynamic response was: 1055 Hz natural frequency, 0.045 viscous damping ratio, and 4.2×10^7 N/m stiffness. Each cut of the 6061-T6 aluminum workpiece was performed using a feed per tooth of 0.10 mm/tooth. The aluminum alloy cutting force coefficients were: $k_{tc} = 792 \times 10^6$ N/m^2, $k_{nc} = 352 \times 10^6$ N/m^2, $k_{te} = 26 \times 10^3$ N/m, and $k_{ne} = 28 \times 10^3$ N/m.

Figures 12–15 display the flexure's feed direction velocity (dx/dt) in the time domain. The continuous signal is displayed as a solid line, while the circles are the once-per-tooth sampled points. In each figure, the left plot shows the simulated behavior and the right plot shows the experimental behavior. Good agreement is observed. The time domain simulation was modified to account

Table 1 Cutting conditions and flexure dynamics for experiments

	Cutting conditions			Flexure dynamics		
Period-n (figure number)	Spindle speed (rpm)	Axial depth, b (mm)	Radial depth (mm)	Stiffness (N/m)	Natural frequency (Hz)	Viscous damping ratio (%)
2 (3)	3486	2.0	1.0	9.0×10^5	83.0	2.00
3 (4)	3800	4.5	5.0	5.6×10^6	163.0	1.08
6 (5)	3200	18.0	1.0	5.6×10^6	202.6	0.28
6 (6)	3250	15.5	1.0	5.6×10^6	205.8	0.28
7 (7)	3200	14.5	1.0	5.6×10^6	204.1	0.28
8 (8)	3310	15.0	2.0	2.1×10^6	130.1	1.47
15 (9)	3200	14.0	1.0	5.6×10^6	204.8	0.28

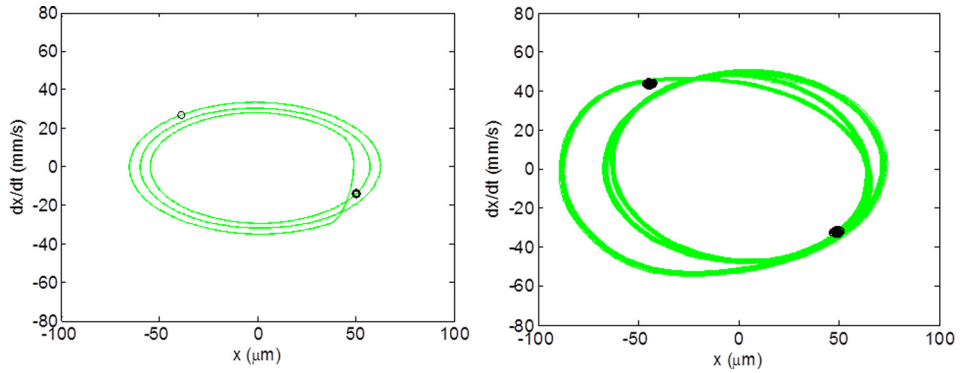

Fig. 3 Poincaré map for period-2 bifurcation. (Left) simulation and (right) experiment.

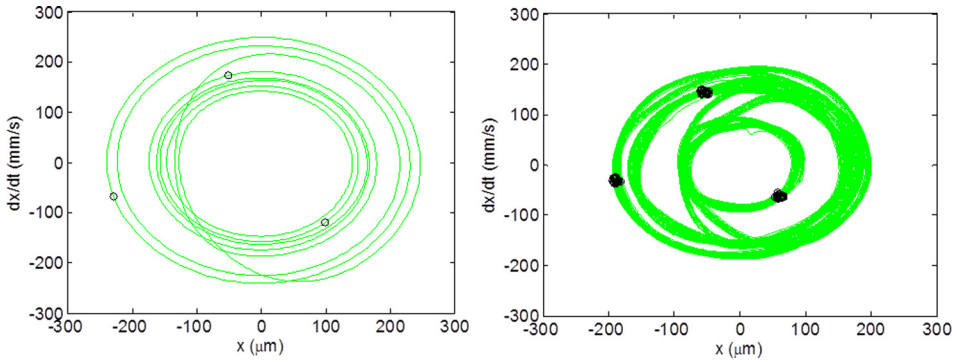

Fig. 4 Poincaré map for period-3 bifurcation. (Left) simulation and (right) experiment. The phase space trajectory is represented by the solid line and the once-per-tooth sampled points are displayed as circles.

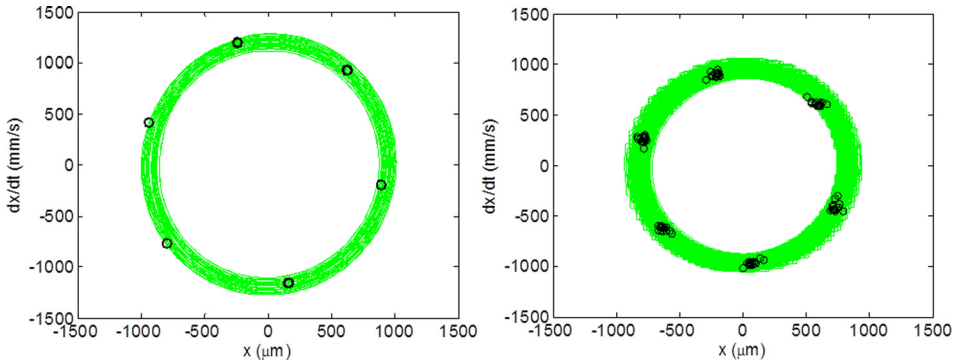

Fig. 5 Poincaré map for period-6 bifurcation. (Left) simulation and (right) experiment.

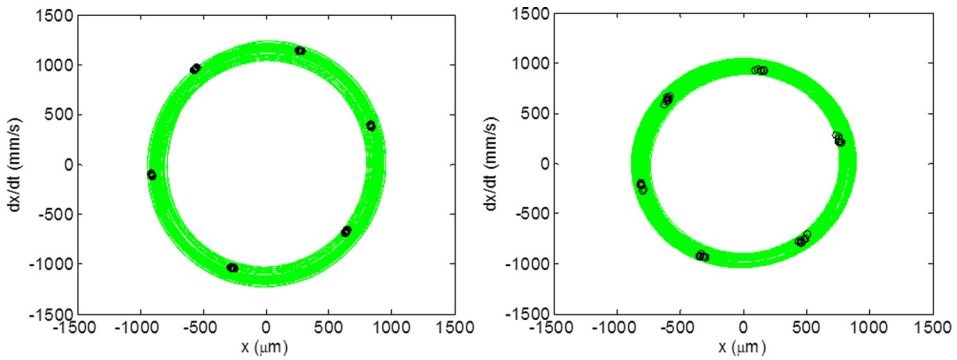

Fig. 6 Poincaré map for a second period-6 bifurcation. (Left) simulation and (right) experiment.

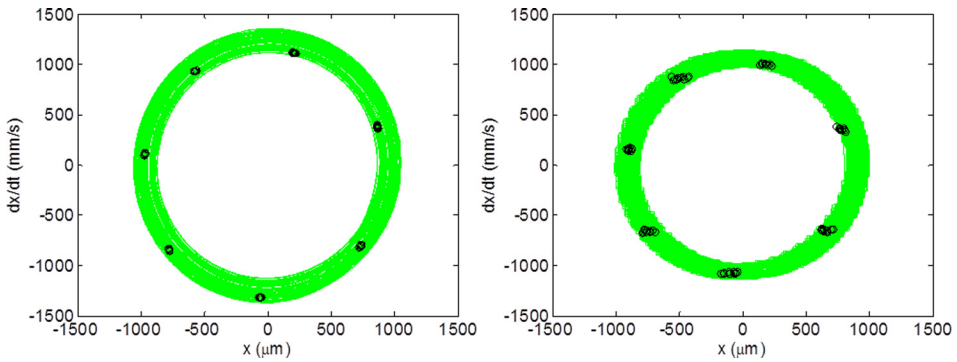

Fig. 7 Poincaré map for period-7 bifurcation. (Left) simulation and (right) experiment.

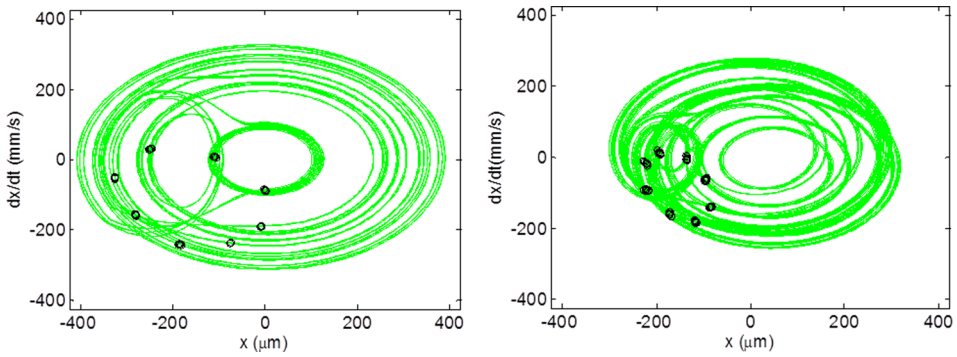

Fig. 8 Poincaré map for period-8 bifurcation. (Left) simulation and (right) experiment.

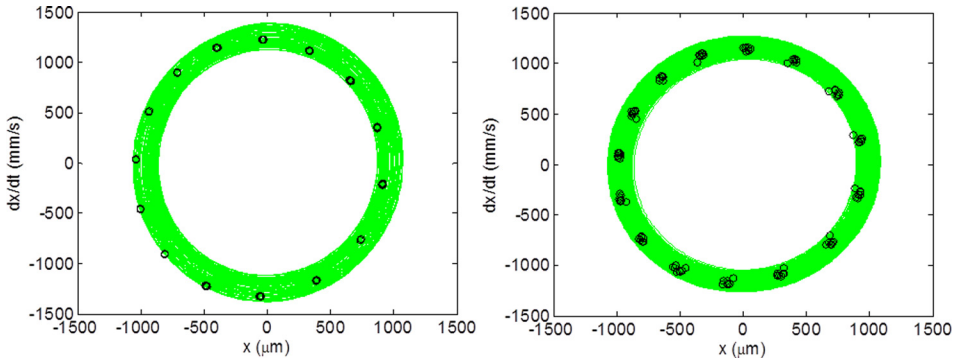

Fig. 9 Poincaré map for period-15 bifurcation. (Left) simulation and (right) experiment.

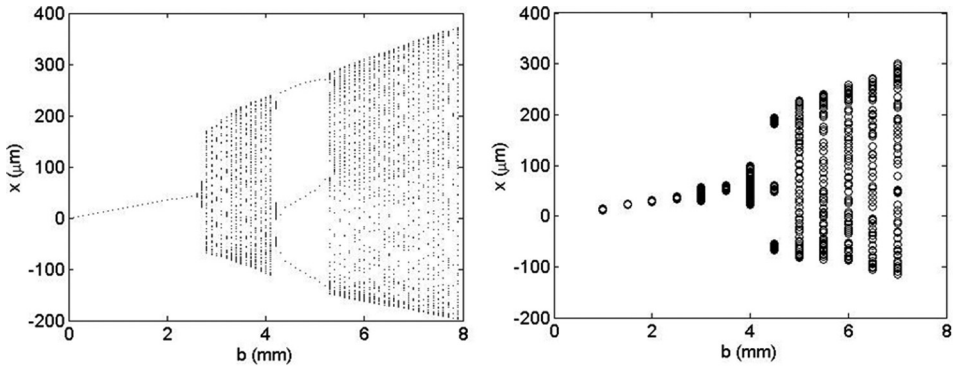

Fig. 10 Bifurcation diagram for 3800 rpm and 5 mm radial depth of cut. (Left) simulation and (right) experiment.

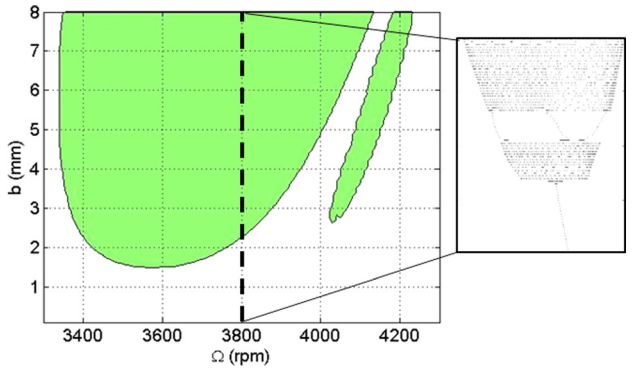

Fig. 11 Simulated stability map for period-3 experimental setup from Table 1 ($M = 1$ μm contour). The transition from stable to unstable behavior occurs at approximately 2.6 mm for a spindle speed of 3800 rpm. The inset shows the bifurcation diagram progression at 3800 rpm from stable to quasi-periodic instability to period-3 and back to quasi-periodic behavior.

for the changing natural frequency due to mass loss. After each time-step, the change in mass was calculated based on the volume of the removed chip and the density of the workpiece material (2700 kg/m^3). This change in mass was then used to update the flexure's natural frequency for the next time-step.

A summary of the behavior seen in Figs. 12–15 is provided here.

(1) Figure 12 exhibits period-6 behavior from 4 to 11 s, followed by quasi-periodic behavior until the end of the cut.
(2) Figure 13 shows period-6 behavior from 4 to 13 s and then quasi-periodic behavior is observed until the end of the cut.
(3) Figure 14 displays quasi-periodic behavior from the beginning of the cut until 11 s and then period-7 behavior from 11 to 15 s.
(4) Figure 15 exhibits quasi-periodic behavior from the beginning of the cut until 8 s, period-15 behavior from 8 to 13 s, and then quasi-periodic behavior until the end of the cut.

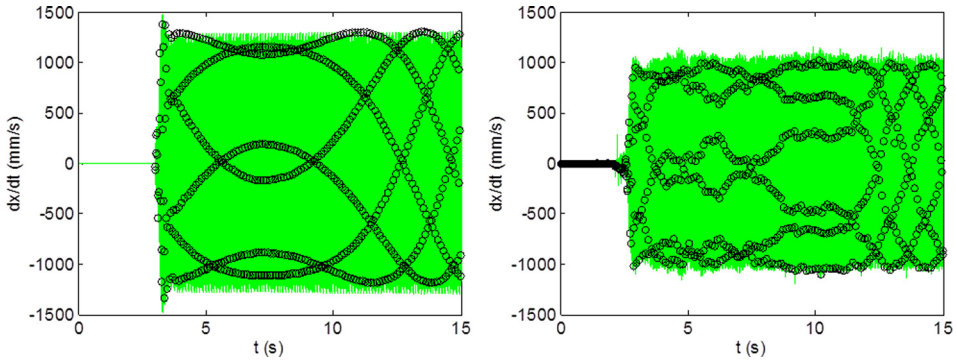

Fig. 12 Variation in bifurcation behavior with changes in natural frequency. Period-6 bifurcation is observed. (Left) simulation and (right) experiment.

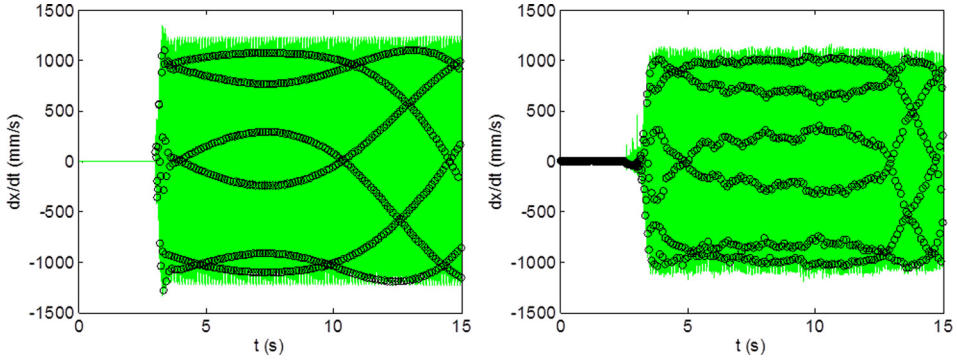

Fig. 13 Variation in bifurcation behavior with changes in natural frequency. Period-6 bifurcation is observed. (Left) simulation and (right) experiment.

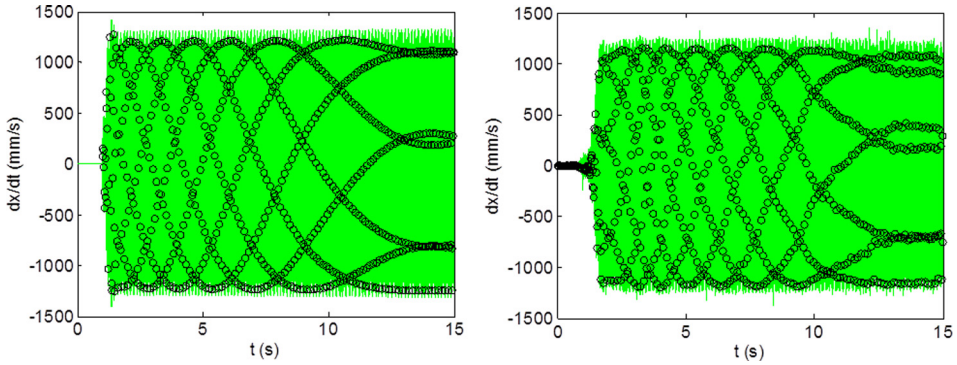

Fig. 14 Variation in bifurcation behavior with changes in natural frequency. Period-7 bifurcation is observed. (Left) simulation and (right) experiment.

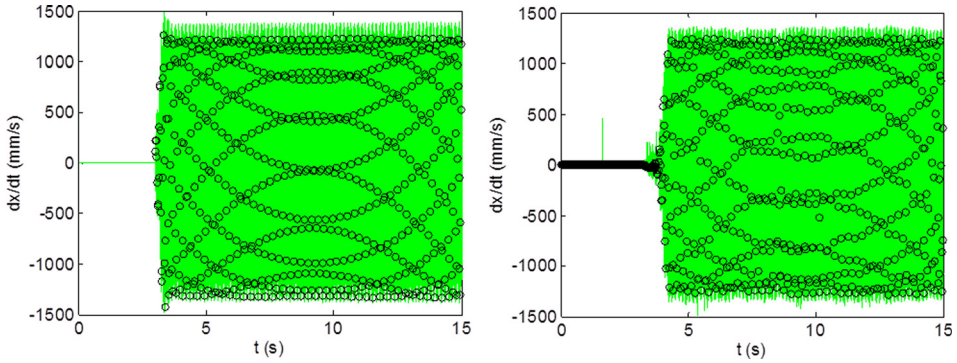

Fig. 15 Variation in bifurcation behavior with changes in natural frequency. Period-15 bifurcation is observed. (Left) simulation and (right) experiment.

Table 2 Changes in flexure natural frequency due to mass removal

	Flexure dynamics				Cutting conditions		
Period-n (figure number)	Natural frequency, beginning of cut (Hz)	Natural frequency, end of cut (Hz)	Change in natural frequency (Hz)	Change in mass (g)	Spindle speed (rpm)	Axial depth, b (mm)	Radial depth (mm)
6 (12)	202.4	202.7	0.3	4.8	3200	18.0	1.0
6 (13)	205.7	205.9	0.2	4.1	3250	15.5	1.0
7 (14)	204.1	204.3	0.2	3.9	3200	14.5	1.0
15 (15)	204.7	204.9	0.2	3.7	3200	14.0	1.0

Sensitivity to Damping

In addition to the changes in bifurcation behavior with natural frequency, the sensitivity to damping was also evaluated. In order to vary the experimental damping, the flexure-based setup displayed in Fig. 2 was replaced with a second flexure to enable adjustable viscous damping. The approach was to add an eddy current damper to the flexure as described in Ref. [49]; see Fig. 16. In the figure, it is seen that a copper conductor is attached to the moving platform. As the conductor moves through the magnetic field generated by the permanent magnets (PM) located on each side, a velocity-dependent force is produced which opposes the motion. The effect is viscous damping that can be increased or decreased by changing the gap between the conductor and magnets.

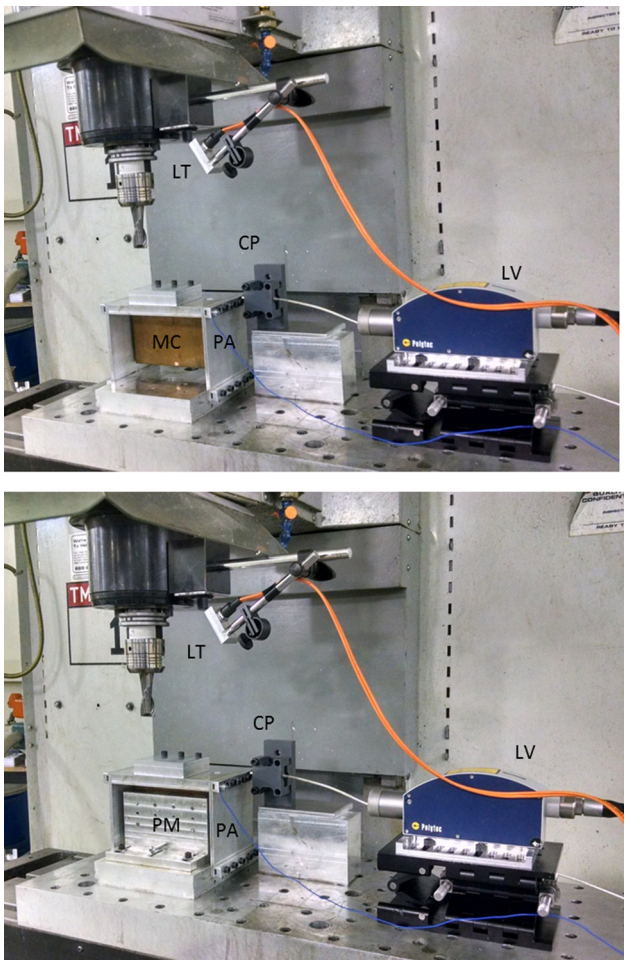

Fig. 16 Milling experimental setup with variable viscous damping. The setup includes a LV, PA, LT, CP, moving conductor, and PM. The top photograph shows the flexure without the PM; the copper conductor is visible inside the parallelogram leaf-type flexure. The lower photograph shows the PM in place. The magnets are positioned on both sides of the copper conductor and provide the eddy current damping effect.

To explore the sensitivity of period-n behavior to damping, machining trials were conducted over a range of axial depths of cut (1 mm to 10 mm) with four different flexure damping values. In all cases, the spindle speed was 3310 rpm, the radial depth of cut was 2 mm, and the feed per tooth was 0.1 mm/tooth. The cutting tool was a 19.1 mm diameter, single flute carbide square end mill (30 deg helix angle): 1055 Hz natural frequency, 0.045 viscous damping ratio, and 4.2×10^7 N/m stiffness. The 6061-T6 aluminum alloy cutting force coefficients were: $k_{tc} = 792 \times 10^6$ N/m^2, $k_{nc} = 352 \times 10^6$ N/m^2, $k_{te} = 26 \times 10^3$ N/m, and $k_{ne} = 28 \times 10^3$ N/m. Table 3 details the tunable flexure dynamics for the four damping values.

Simulated and experimental bifurcation diagrams are presented in Figs. 17–20 for the dynamics defined in Table 3. It is observed that as the damping increases, the region of period-2 behavior diminishes in size and, in Fig. 20 with a damping ratio of 3.55%, it disappears all together. The stable behavior persists up to an axial depth of approximately 4 mm for Figs. 17–19. The period-2 behavior is then seen for decreasing ranges of axial depth as the damping increases. It continues to approximately 8.2 mm for 1.47%, to approximately 7.6 mm for 1.91%, and to approximately 6.8 mm for 2.34%. In all cases, the period-2 behavior is followed by a second stable zone at higher axial depths.

To observe the global behavior, stability maps were generated using the same time domain simulation implemented to construct Figs. 17–20. The spindle speed range was 2600 rpm to 3800 rpm in steps of 20 rpm and the axial depth range was 0.2 mm to 10 mm in steps of 0.2 mm. The results are presented in Figs. 21–24, where a vertical line is added to each figure at 3310 rpm to indicate the position of the bifurcation diagrams in Figs. 18–20. The stability metric defined in Eq. 1 was used to identify stable and unstable conditions for each grid point.

Conclusions

This paper presented numerical and experimental analyses of milling bifurcations, or instabilities. Numerical simulation was used to solve the time-delay equations of motions that describe milling behavior. Once-per-tooth period sampling was employed to study the stability behavior, including period-n bifurcations, using Poincaré maps. Bifurcation diagrams and stability maps were also presented. The numerical predictions were verified by experiments, where milling vibration amplitudes were measured for both stable and unstable conditions using flexure-based setups. The vibration signals were also sampled once-per-tooth period to

Table 3 Flexure dynamics for damping sensitivity experiments

Period-n (figure number)	Stiffness (N/m)	Natural frequency (Hz)	Viscous damping ratio (%)
2 (17)	2.1×10^6	130.0	1.47
2 (18)	2.1×10^6	130.0	1.91
2 (19)	2.1×10^6	130.0	2.34
- (20)	2.1×10^6	130.0	3.55

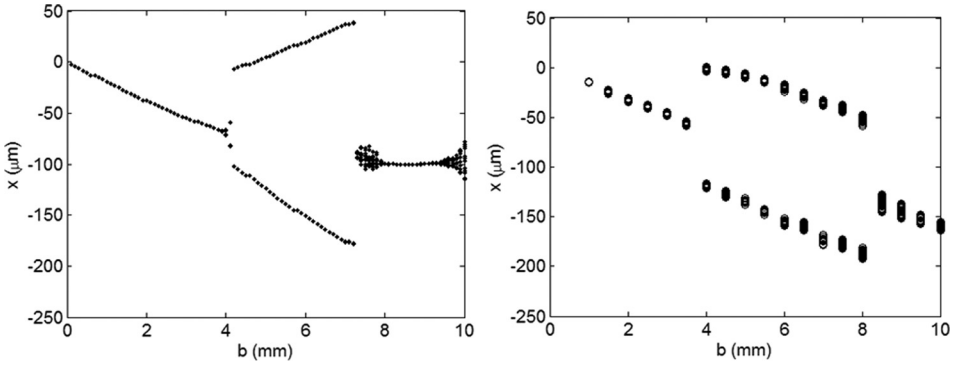

Fig. 17 Bifurcation diagram for 1.47% damping (3310 rpm). (Left) simulation and (right) experiment. Stable behavior is observed up to approximately 4 mm, period-2 behavior then occurs up to approximately 8 mm, then stable behavior is again seen.

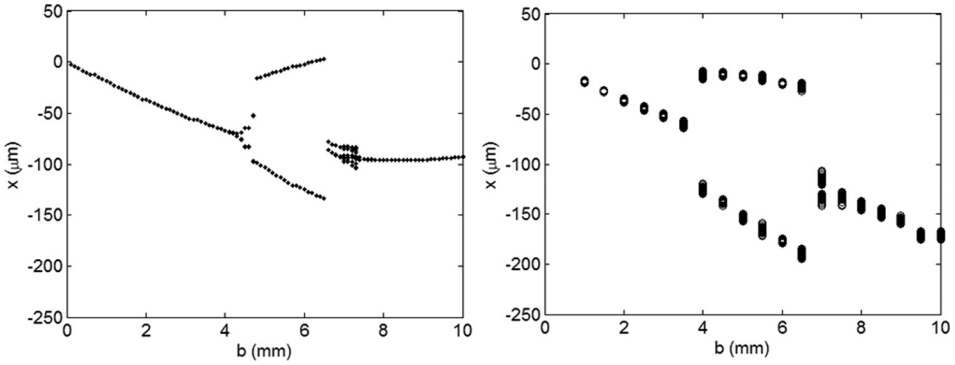

Fig. 18 Bifurcation diagram for 1.91% damping (3310 rpm). (Left) simulation and (right) experiment.

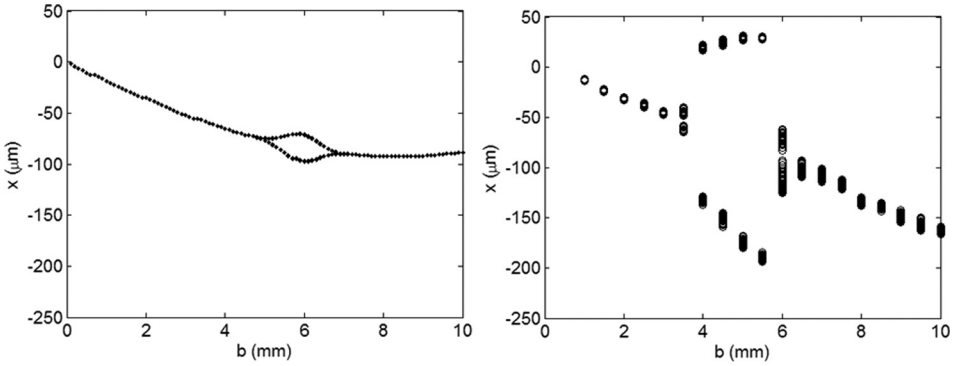

Fig. 19 Bifurcation diagram for 2.34% damping (3310 rpm). (Left) simulation and (right) experiment.

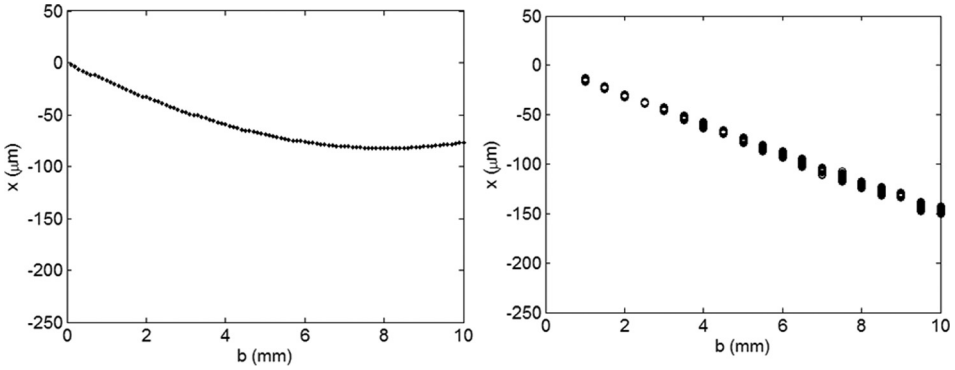

Fig. 20 Bifurcation diagram for 3.55% damping (3310 rpm). (Left) simulation and (right) experiment.

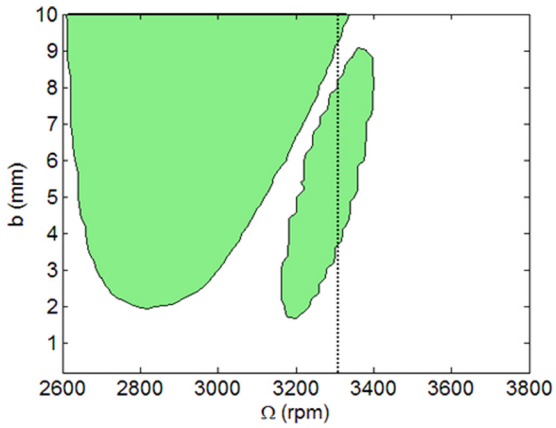

Fig. 21 Simulated stability map for 1.47% damping ($M = 1$ μm contour). As the axial depth is increased, the transition from stable to period-2 (3.8 mm), period-2 back to stable (8.2 mm), and stable to quasi-periodic behavior (9.2 mm) is observed.

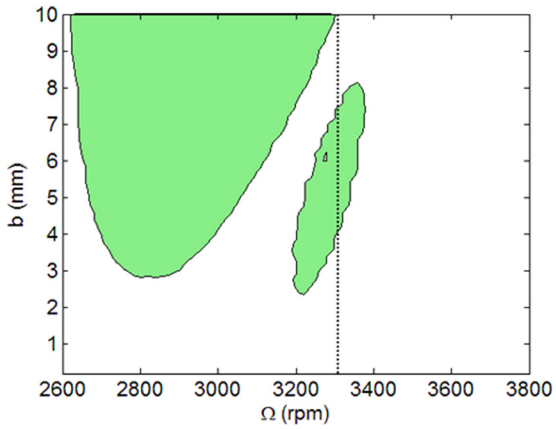

Fig. 22 Simulated stability map for 1.91% damping ($M = 1$ μm contour). As the axial depth is increased, the transition from stable to period-2 (4.2 mm) and period-2 back to stable (7.6 mm) is observed.

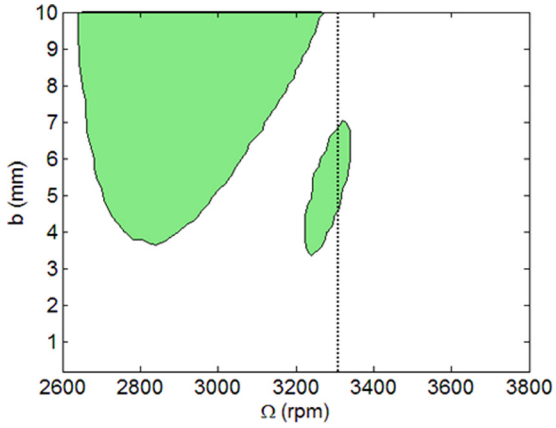

Fig. 23 Simulated stability map for 2.34% damping ($M = 1$ μm contour). As the axial depth is increased, the transition from stable to period-2 (4.6 mm) and period-2 back to stable (6.8 mm) is observed.

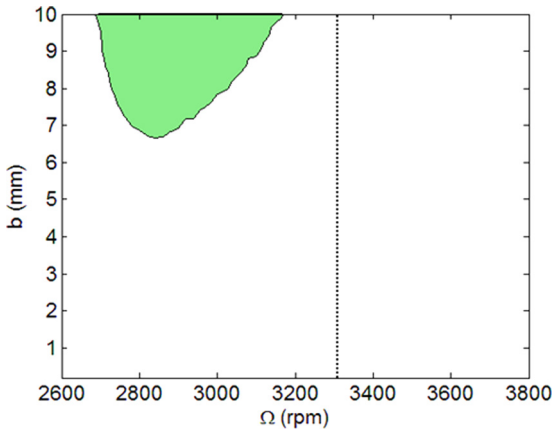

Fig. 24 Simulated stability map for 3.55% damping ($M = 1$ μm contour). Stable behavior is observed at all axial depths.

construct experimental Poincaré maps and bifurcation diagrams. The sensitivity of milling bifurcations to changes in natural frequency and damping were predicted. It was observed that the bifurcation behavior exhibited significant sensitivity to changes in the structural dynamics.

Acknowledgment

This material is based upon the work supported by the National Science Foundation under Grant No. CMMI-1561221.

References

[1] Arnold, R. N., 1946, "The Mechanism of Tool Vibration in the Cutting of Steel," Institute of Mechanical Engineers, **154**(1), pp. 261–284.
[2] Doi, S., and Kato, S., 1956, "Chatter Vibration of Lathe Tools," Trans. ASME, **78**, pp. 1127–1134.
[3] Tobias, S. A., and Fishwick, W., 1958, "The Chatter of Lathe Tools Under Orthogonal Cutting Conditions," Trans. ASME, **80**, pp. 1079–1088.
[4] Tlusty, J., and Polacek, M., 1963, "The Stability of Machine Tools Against Self-Excited Vibrations in Machining," Proceedings of the ASME International Research in Production Engineering, pp. 465–474.
[5] Tobias, S. A., 1965, *Machine Tool Vibration*, Wiley, New York.
[6] Merritt, H. E., 1965, "Theory of Self-Excited Machine-Tool Chatter," ASME J. Eng. Ind., **87**(4), pp. 447–454.
[7] Tlusty, J., and Polacek, M., 1968, "Experience With Analysing Stability of Machine Tool Against Chatter," 9th MTDR Conference, pp. 521–570.
[8] Shridar, R., Hohn, R. E., and Long, G. W., 1968, "A General Formulation of the Milling Process Equation," ASME J. Eng. Ind., **90**(2), pp. 317–324.
[9] Hohn, R. E., Shridar, R., and Long, G. W., 1968, "A Stability Algorithm for a Special Case of the Milling Process," ASME J. Eng. Ind., **90**(2), pp. 326–329.
[10] Shridar, R., Hohn, R. E., and Long, G. W., 1968, "A Stability Algorithm for the General Milling Process," ASME J. Eng. Ind., **90**(2), pp. 330–334.
[11] Hanna, N. H., and Tobias, S. A., 1974, "A Theory of Nonlinear Regenerative Chatter," ASME J. Eng. Ind., **96**(1), pp. 247–255.
[12] Tlusty, J., and Ismail, F., 1981, "Basic Non-Linearity in Machining Chatter," Ann. CIRP, **30**(1), pp. 299–304.
[13] Tlusty, J., and Ismail, F., 1983, "Special Aspects of Chatter in Milling," ASME J. Vib. Acoust. Stress Reliab. Des., **105**(1), pp. 24–32.
[14] Tlusty, J., 1985, "Machine Dynamics," *Handbook of High-Speed Machining Technology*, R. I. King, ed., Chapman and Hall, New York, pp. 48–153.
[15] Tlusty, J., 1986, "Dynamics of High-Speed Milling," ASME J. Eng. Ind., **108**(2), pp. 59–67.
[16] Minis, I., and Yanusevsky, R., 1993, "A New Theoretical Approach for Prediction of Chatter in Milling," ASME J. Eng. Ind., **115**(1), pp. 1–8.
[17] Altintas, Y., and Budak, E., 1995, "Analytical Prediction of Stability Lobes in Milling," Ann. CIRP, **44**(1), pp. 357–362.
[18] Davies, M. A., Dutterer, B. S., Pratt, J. R., and Schaut, A. J., 1998, "On the Dynamics of High-Speed Milling With Long, Slender Endmills," Ann. CIRP, **47**(1), pp. 55–60.
[19] Moon, F. C., and Kalmár-Nagy, T., 2001, "Nonlinear Models for Complex Dynamics in Cutting Materials," Philos. Trans. R. Soc. London A, **359**(1781), pp. 695–711.
[20] Davies, M. A., Pratt, J. R., Dutterer, B. S., and Burns, T. J., 2000, "The Stability of Low Radial Immersion Milling," Ann. CIRP, **49**(1), pp. 37–40.
[21] Moon, F. C., 1994, "Chaotic Dynamics and Fractals in Material Removal Processes," *Nonlinearity and Chaos in Engineering Dynamics*, J. Thompson, and S. Bishop, eds., Wiley, New York.

[22] Bukkapatnam, S., Lakhtakia, A., and Kumara, S., 1995, "Analysis of Senor Signals Shows Turning on a Lathe Exhibits Low-Dimensional Chaos," Phys. Rev. E, **52**(3), pp. 2375–2387.
[23] Stépán, G., and Kalmár-Nagy, T., 1997, "Nonlinear Regenerative Machine Tool Vibrations," ASME Paper No. DETC 97/VIB-4021.
[24] Nayfey, A., Chin, C., and Pratt, J., 1998, "Applications of Perturbation Methods to Tool Chatter Dynamics," *Dynamics and Chaos in Manufacturing Processes*, F. C. Moon, ed., Wiley, New York.
[25] Minis, I., and Berger, B. S., 1998, "Modelling, Analysis, and Characterization of Machining Dynamics," *Dynamics and Chaos in Manufacturing Processes*, F. C. Moon, ed., Wiley, New York.
[26] Moon, F. C., and Johnson, M., 1998, "Nonlinear 2 and Chaos in Manufacturing Processes," *Dynamics and Chaos in Manufacturing Processes*, F. C. Moon, ed., Wiley, New York.
[27] Smith, K. S., and Tlusty, J., 1991, "An Overview of Modeling and Simulation of the Milling Process," J. Eng. Ind., **113**(2), pp. 169–175.
[28] Campomanes, M. L., and Altintas, Y., 2003, "An Improved Time Domain Simulation for Dynamic Milling at Small Radial Immersions," ASME J. Manuf. Sci. Eng., **125**(3), pp. 416–422.
[29] Zhao, M. X., and Balachandran, B., 2001, "Dynamics and Stability of Milling Process," Int. J. Solids Struct., **38**(10–13), pp. 2233–2248.
[30] Davies, M. A., Pratt, J. R., Dutterer, B., and Burns, T. J., 2002, "Stability Prediction for Low Radial Immersion Milling," ASME J. Manuf. Sci. Eng., **124**(2), pp. 217–225.
[31] Mann, B. P., Insperger, T., Bayly, P. V., and Stépán, G., 2003, "Stability of Up-Milling and Down-Milling—Part 2: Experimental Verification," Int. J. Mach. Tools Manuf., **43**(1), pp. 35–40.
[32] Mann, B. P., Insperger, T., Bayly, P. V., and Stépán, G., 2003, "Stability of Up-Milling and Down-Milling—Part 1: Alternative Analytical Methods," Int. J. Mach. Tools Manuf., **43**(1), pp. 25–34.
[33] Insperger, T., Stépán, G., Bayly, P. V., and Mann, B. P., 2003, "Multiple Chatter Frequencies in Milling Processes," J. Sound Vib., **262**(2), pp. 333–345.
[34] Insperger, T., and Stépán, G., 2004, "Vibration Frequencies in High-Speed Milling Processes or A Positive Answer to Davies, Pratt, Dutterer, and Burns," ASME J. Manuf. Sci. Eng., **126**(3), pp. 481–487.
[35] Mann, B. P., Bayly, P. V., Davies, M. A., and Halley, J. E., 2004, "Limit Cycles, Bifurcations, and Accuracy of the Milling Process," J. Sound Vib., **277**(1–2), pp. 31–48.
[36] Merdol, S. D., and Altintas, Y., 2004, "Multi Frequency Solution of Chatter Stability for Low Immersion Milling," ASME J. Manuf. Sci. Eng., **126**(3), pp. 459–466.
[37] Govekar, E., Gradišek, J., Kalveram, M., Insperger, T., Weinert, K., Stepan, G., and Grabec, I., 2005, "On Stability and Dynamics of Milling at Small Radial Immersion," Ann. CIRP, **54**(1), pp. 357–362.
[38] Gradišek, J., Kalveram, M., Insperger, T., Weinert, K., Stépán, G., Govekar, E., and Grabec, I., 2005, "On Stability Prediction for Milling," Int. J. Mach. Tools Manuf., **45**(7–8), pp. 769–781.
[39] Mann, B. P., Garg, N. K., Young, K. A., and Helvey, A. M., 2005, "Milling Bifurcations From Structural Asymmetry and Nonlinear Regeneration," Nonlinear Dyn., **42**(4), pp. 319–337.
[40] Stépán, G., Szalai, R., Mann, B. P., Bayly, P. V., Insperger, T., Gradisek, J., and Govekar, E., 2005, "Nonlinear Dynamics of High-Speed Milling—Analyses, Numerics, and Experiments," ASME J. Vib. Acoust., **127**(2), pp. 197–203.
[41] Zatarain, M., Muñoa, J., Peigné, G., and Insperger, T., 2006, "Analysis of the Influence of Mill Helix Angle on Chatter Stability," Ann. CIRP, **55**(1), pp. 365–368.
[42] Insperger, T., Munoa, J., Zatarain, M. A., and Peigné, G., 2006, "Unstable Islands in the Stability Chart of Milling Processes Due to the Helix Angle," CIRP 2nd International Conference on High Performance Cutting, Vancouver, Canada, June 12–13, pp. 12–13.
[43] Patel, B. R., Mann, B. P., and Young, K. A., 2008, "Uncharted Islands of Chatter Instability in Milling," Int. J. Mach. Tools Manuf., **48**(1), pp. 124–134.
[44] Schmitz, T., and Smith, K. S., 2009, *Machining Dynamics: Frequency Response to Improved Productivity*, Springer, New York.
[45] Honeycutt, A., and Schmitz, T., 2016, "A New Metric for Automated Stability Identification in Time Domain Milling Simulation," ASME J. Manuf. Sci. Eng., **138**(7), p. 074501.
[46] Schmitz, T., Davies, M., Medicus, K., and Snyder, J., 2001, "Improving High-Speed Machining Material Removal Rates by Rapid Dynamic Analysis," Ann. CIRP, **50**(1) pp. 263–268.
[47] Schmitz, T., Medicus, K., and Dutterer, B., 2002, "Exploring Once-Per-Revolution Audio Signal Variance as a Chatter Indicator," Mach. Sci. Technol., **6**(2), pp. 215–233.
[48] Schmitz, T., 2003, "Chatter Recognition by a Statistical Evaluation of the Synchronously Sampled Audio Signal," J. Sound Vib., **262**(3), pp. 721–730.
[49] Ransom, T., Honeycutt, A., and Schmitz, T., 2016, "A New Tunable Dynamics Platform for Milling Experiments," Precis. Eng., **44**, pp. 252–256.